Catalysis Science & Technology

PAPER

View Article Online
View Journal | View Issue

Cite this: *Catal. Sci. Technol.*, 2019, 9, 2469

Oxidative dehydrogenation of ethylbenzene to styrene over the $CoFe_2O_4$–MCM-41 catalyst: preferential adsorption on the $O^{2-}Fe^{3+}O^{2-}$ sites located at octahedral positions†

Moisés da Costa Borges Soares,[a] Felipe Fernandes Barbosa,[a] Marco Antonio Morales Torres,[b] Antoninho Valentini,[c] Anderson dos Reis Albuquerque,[d] Julio Ricardo Sambrano,[e] Sibele B. C. Pergher,[a] Nadine Essayem[f] and Tiago Pinheiro Braga *[a]

The present study describes the catalytic performance of cobalt ferrite supported on MCM-41 for the oxidative dehydrogenation of ethylbenzene. The catalytic activity of cobalt ferrite was compared with that of the traditional hematite based catalyst. A mechanism is described indicating the role of the O^{2-}–Fe^{3+}–O^{2-} and O^{2-}–Co^{2+}–O^{2-} acid–base sites present in the tetrahedral and octahedral positions of the cobalt ferrite structure. The solids were characterized by X-ray diffraction (XRD), Raman spectroscopy (RS), Mössbauer spectroscopy (MS), X-ray photoelectron spectroscopy (XPS), vibrating-sample magnetometry (VSM), temperature-programmed reduction (H_2-TPR), chemical adsorption of NO and pyridine followed by infrared analysis, temperature programmed desorption of CO_2 (TPD), N_2 physisorption and transmission electronic microscopy (TEM). The catalytic tests were performed in a fixed bed reactor using a saturator containing ethylbenzene. The XRD, RS, MS and VSM results confirmed the formation of cobalt ferrite, which was classified as partially inverted ferrite. The low-angle XRD, N_2 isotherms and TEM images show the formation of the mesoporous MCM-41 support with a high surface area. The catalytic tests confirmed that the cobalt ferrite is more active and stable than the traditional hematite catalyst. The catalytic cycle for ethylbenzene dehydrogenation occurs preferentially in the O^{2-}–Fe^{3+}–O^{2-} octahedral sites compared to the O^{2-}–Co^{2+}–O^{2-} sites. A theoretical approach using density functional theory revealed a higher acidity of iron sites compared to cobalt ones on the surface of the partially inverted spinel. The adsorption of ethylbenzene takes place preferentially in the outermost FeO_x ($x > 4$) sites (Lewis acid) and the dehydrogenation reaction occurs predominantly in the oxygens bound to iron (Lewis base) according to the complementary electrostatic potential surface approach.

Received 1st April 2019,
Accepted 10th April 2019

DOI: 10.1039/c9cy00618d

rsc.li/catalysis

1. Introduction

Catalytic dehydrogenation of ethylbenzene is the most applied industrial process to produce styrene, which is a precursor for the production of polymers, including polystyrene and styrene–butadiene rubber.[1] In industry, this reaction is generally conducted over iron oxide-based catalysts with an excess supply of steam at high temperature (endothermic process).[2]

Several studies have been carried out using commercial catalysts containing Fe_2O_3 as the main active site.[3–5] However, there are several issues related to the use of superheated steam and concerning the Fe_2O_3 sites. The generation of steam occurs with a great loss of energy in the gas–liquid separator and the equilibrium conversion is low even at high reaction temperatures.[6] Furthermore, although a commercial Fe_2O_3-based catalyst presents reasonable activity and

[a] *Laboratório de Peneiras Moleculares (LABPEMOL), Instituto de Química, Universidade Federal do Rio Grande do Norte, 59078-970, Natal, RN, Brazil. E-mail: tiagoquimicaufrn@gmail.com*
[b] *Departamento de Física, Universidade Federal do Rio Grande do Norte, 59078-970, Natal, RN, Brazil*
[c] *Langmuir - Laboratório de Adsorção e Catálise, Departamento de Química Analítica e Físico-Química, Universidade Federal do Ceará, Campus do Pici, CEP, 60455-970, Fortaleza, CE, Brazil*
[d] *Instituto de Química, Universidade Federal do Rio Grande do Norte, 59078-970, Natal, RN, Brazil*
[e] *Grupo de Modelagem e Simulação Molecular, INCTMN-UNESP, São Paulo State University, CEP, 17033-360, Bauru, SP, Brazil*
[f] *Institut de recherches sur la catalyse et l'environnement, 2 Av. A. Einstein, 69626 Villeurbanne Cedex, France*

† Electronic supplementary information (ESI) available. See DOI: 10.1039/c9cy00618d

selectivity as well as low cost, the solid has very low stability leading to deactivation during the reaction. The deactivation is mainly due to chemical reduction of Fe^{3+} (major site) and coke deposition.[7]

Several investigations are being done in order to develop alternative processes to the steam process and to find active sites that are more resistant to a reducing atmosphere.[8–12] The substitution of $H_2O(g)$ by $CO_2(g)$ as a soft oxidant during the oxidative dehydrogenation of ethylbenzene is an interesting alternative, since it minimizes the thermodynamic limitation of the commercial process, reduces energy expenditure and generates a commercial value for CO_2, one of the gases causing the greenhouse effect.[8]

Oxides with high structural stability such as perovskites and spinels have higher catalytic stability, minimizing the deactivation by phase change and carbon deposition compared to conventional hematite under hard reaction conditions.[9–12] Madduluri *et al.* synthesized $MgAl_2O_4$ spinel based-catalysts and applied them in the oxidative dehydrogenation of ethylbenzene. It was confirmed that the presence of Fe in the spinel phase has a synergistic effect with promising catalytic properties compared to the classical Fe_2O_3 catalyst.[9] Ji *et al.* presented the synthesis of an Fe-doped $MgAl_2O_4$ spinel catalyst for ethylbenzene dehydrogenation in the presence of CO_2. The results showed that the catalytic performance of Fe^{3+} in the spinel is superior to traditional α-Fe_2O_3, and the synergistic effect between Fe^{2+} and Fe^{3+} increases the catalytic activity.[10]

Watanabe *et al.* prepared the $La_{0.8}Ba_{0.2}Fe_{0.4}Mn_{0.6}O_{3-\gamma}$ perovskite based-oxide. The results indicated that this type of solid is highly resistant to the reaction conditions and consequently shows extremely high activity and stability for ethylbenzene dehydrogenation to produce styrene.[11] Watanabe *et al.* showed that the $BaFe_{0.02}Zr_{0.98}O_3$ perovskite based-solid presented a higher styrene yield than the classic Fe_2O_3–K catalyst, confirming the high stability of the perovskite structure.[12]

Spinel-type ferrites (MFe_2O_4) are structures with Fe^{3+} and lattice oxygen, the major sites for oxidative dehydrogenation of ethylbenzene, have high structural stability and present a relatively simple structure and easy stoichiometric control compared to iron-based perovskites. Fe^{3+} and M^{2+} may occupy tetrahedral and octahedral positions in the crystal lattice, since these spinel ferrites are classified as normal or inverse spinel structures. In the case of normal spinels, all the divalent metal ions (M^{2+}) occupy the tetrahedral sites and all the trivalent iron ions (Fe^{3+}) occupy the octahedral sites, while in inverse spinels the divalent metal ion totally occupies the octahedral (B) site and the trivalent iron ions are equally distributed between the tetrahedral (A) and octahedral (B) sites.[13] Specifically, the cobalt ferrite may be an inverse or partially inverse spinel depending on the cation substitution, which is directly related to the synthesis conditions. The Co^{2+} and Fe^{3+} distribution between A-sites and B sites has an influence on the physical properties of the $CoFe_2O_4$ structure and consequently on the catalytic properties.[14]

Ferrites as catalysts for the oxidative dehydrogenation of ethylbenzene are rarely described in the literature.[15,16] There are few experimental studies, and these do not detail the surface chemistry involved in the catalytic cycle. A mechanistic proposal that takes into account the adsorption of ethylbenzene in the ferrite's tetrahedral and/or octahedral sites, indicating the preferred ethylbenzene adsorption sites, remains an open search field.

On the other hand, it is known that according to the synthesis conditions[17,18] some spinel particles may exhibit selected surfaces with enhanced catalytic activity. Some studies in cubic spinels have presented the {001} surface as the thermodynamically most stable, and consequently the most representative for theoretical modelling.[19,20]

Furthermore, it is important to mention that the physicochemical properties of the support directly affect the catalytic performance for the oxidative dehydrogenation of ethylbenzene using iron based solids.[21] Among the different supports, MCM-41 is the most well-studied member of the family of mesostructured materials M41S, which presents a high surface area, well-ordered cylindrical channels with a hexagonal arrangement and controllable uniform pore sizes of 2–10 nm.[22] Few studies show the dehydrogenation of ethylbenzene using hematite dispersed in MCM-41.[22–24] However, to the best of our knowledge, this is the first investigation on $CoFe_2O_4$ dispersed in MCM-41 as a catalyst for oxidative dehydrogenation of ethylbenzene in the presence of carbon dioxide.

Thus, the present study shows the synthesis of the $CoFe_2O_4$–MCM-41 catalyst, and its characterization in order to obtain information about the physical–chemical properties of the ferrite (structure, chemical surface, magnetism, acidity–basicity, texture, redox, and morphology) and the catalytic performance for the conversion of ethylbenzene to styrene in the presence of CO_2. Finally, a mechanistic approach taking into account the Fe^{3+} and Co^{2+} ions in the tetrahedral and octahedral sites of the cobalt ferrite, was presented and the results were supported by a DFT (density functional theory) computational study. The first-principles study provided valuable insights into the effect of each cation on the particle's surfaces. Furthermore, the influence of Fe and Co on the electronic structure of the (001) surface of the $CoFe_2O_4$ particles was investigated.

2. Experimental

2.1. Synthesis of the silica MCM-41 support

The synthesis of the mesoporous silica MCM-41 support was based on a method previously described.[25] The synthesis uses the following molar ratio, $1SiO_2 : 0.15CTABr : 0.26TMAOH : 20.52H_2O$. Initially, 100.53 g of distilled water and 15 g of CTABr were added to a plastic beaker at room temperature under constant stirring for 1 h. Meanwhile, another solution containing 25.95 g of 25% TMAOH and 2.88 g of silica aerosol was prepared in another plastic beaker under magnetic stirring for 1 h to homogenize the solution. Subsequently, both solutions were mixed in a plastic beaker. This new solution was slowly added to 13.56 g of aerosil silica and mixed for 1 h until the formation of a homogenous gel. Afterward,

the gel was transferred to Teflon-lined stainless steel autoclaves and kept at 135 °C for 24 h. Then, the formed material was filtered and dried at 100 °C for 12 h. Finally, the obtained precursor was calcined at 550 °C for 6 h using synthetic air. The final sample was named as pure MCM-41.

2.2. Synthesis of $CoFe_2O_4$ dispersed on the silica MCM-41 support by incipient wetness impregnation

The synthesis of 20 wt% $CoFe_2O_4$/MCM-41 and 20 wt% Fe_2O_3/MCM-41 catalysts was carried out by the classical incipient wetness impregnation method. For the $CoFe_2O_4$/MCM-41 solid, an aqueous solution of iron nitrate $\{Fe(NO_3)_3{\cdot}9H_2O$ – 404 g $mol^{-1}\}$ and cobalt nitrate $\{Co(NO_3)_2{\cdot}6H_2O$ – 290.7 g $mol^{-1}\}$ precursors was used. 1.0 g of MCM-41 was mixed with an aqueous solution containing the appropriate quantity of iron nitrate and/or cobalt nitrate. Afterward, the samples were dried at 100 °C for 12 h and, finally, calcined under air at 700 °C for 2 h to obtain the cobalt ferrite for 20 wt% $CoFe_2O_4$/MCM-41 and hematite for 20 wt% Fe_2O_3/MCM-41. The samples 20 wt% $CoFe_2O_4$/MCM-41 and 20 wt% Fe_2O_3/MCM-41 were labeled as CF-MCM-41 and Fe_2O_3-MCM-41, respectively.

2.3. Characterization of the solids

The chemical composition of the catalyst was determined using X-ray fluorescence (XRF) spectroscopy with a ZSX mini II spectrometer (Rigaku).

The X-ray diffractograms were obtained on a Bruker D2 Phaser diffractometer equipped with a CuKα radiation source (λ = 1.54 Å) with a Ni filter, with a step of 0.02° and an angle (2θ) range from 10 to 90°, using a Lynxeye detector to determine the crystal structure of the cobalt ferrite or hematite. Phase identification was done using the X-Pert HighScore Panalytical software and the JCPDS-ICDD 2003 database.[26] Rietveld refinements were performed using the GSAS software[27] and an EXPGUI interface[28] after determining the instrumental broadening by means of refining a LaB6 NIST standard sample. The modified pseudo-Voigt function (Thompson–Cox–Hastings) was chosen to adjust the profiles of the diffraction peaks for the identified crystalline phases. The full width at half maximum (FWHM) of the peaks was used to calculate the crystallite size based on the Scherrer equation.[29]

Raman spectroscopy investigations were conducted at room temperature using a Raman microscope (HORIBA Scientific, LabRAM HR Evolution model) with a 532 nm excitation source from an Ar + laser in order to identify the $CoFe_2O_4$ and α-Fe_2O_3 phases.

^{57}Fe Mössbauer spectra were recorded in the transmission mode using a spectrometer (SEECo) with triangular velocity sweep. A helium closed cycle variable temperature cryostat (Janis) was used to record the spectra at 12 K and 300 K. The 14.4 keV γ-radiation source is ^{57}Co in a Rh matrix with an activity of 20 mCi.

XPS analyses were performed on a Kratos Ultra DLD spectrometer using monochromated Al Kα radiation (10 mA, 15 kV). All spectra were taken in the hybrid (combined electrostatic and magnetic lens) mode. All spectra were referenced to the C 1s line at binding energy 284.6 eV, characteristic of ever-present adventitious carbon (C–C and C–H). This peak position was obtained after Shirley background subtraction and decomposition of the C 1s peak envelope using a Gaussian–Lorentzian (70–30%) curve fit. All other photoelectron peaks were background-subtracted and fitted in the same manner. Quantification was performed using the VISION software supplied. The relative sensitivity factors (RSFs) applied are inherent to this software and incorporate Wagner photoelectron cross-sections and analyser transmission correction.

Isothermal hysteresis loop ($M \times H$), zero field cooling (Mzfc) and field cooling (Mfc) magnetic measurements as a function of temperature were performed using a physical property measurement system (PPMS-Dynaccol, Quantum Design) equipped with a vibrating sample magnetometer (VSM).

Temperature-programmed reduction (TPR) analyses were performed in the range of 100–950 °C in a quartz reactor using an 8% H_2/N_2 mixture flow (20 mL min^{-1}) at a heating rate of 10 °C min^{-1}. A thermal conductivity detector (TCD) was used to follow the H_2 consumption and determine the resistance of the materials to the reducing atmosphere and the redox properties.

The FTIR spectra of self-supported pellets of CF-MCM-41-based catalysts were recorded with a Bruker Vector 22 spectrometer in the absorption mode with a resolution of 2 cm^{-1}. The catalysts were placed in an IR cell equipped with CaF_2 windows and treated *in situ*. The different solids were first pretreated at 450 °C under vacuum for 1 h. Pyridine was adsorbed under saturation vapor pressure for 5 min at room temperature and the pellet was desorbed at 150 °C for 1 h in order to remove the physisorbed pyridine species. The sample's spectra after pretreatment and after pyridine adsorption were recorded in order to evaluate the acidic properties of the solids.

Before adsorption, NO was further purified by passing through a liquid nitrogen cold trap and additional fraction distillation. Initially, the catalysts were heated at 450 °C under vacuum for 3 h as the pretreatment. The adsorption time is set as 5 min for all the FTIR experiments using a pressure of 20 Torr at room temperature. Subsequently, NO was adsorbed for 18 h using 20 Torr at 200 °C. Subtractions of the IR spectra of the catalyst wafer under vacuum before adding NO and the NO gas phase spectra to catalyst wafer under a NO atmosphere were performed in order to evaluate the surface chemistry of the acid sites present in the catalysts. After adsorption and before FTIR analysis, the samples were subjected to a vacuum at room temperature.

The CO_2 temperature-programmed desorption (TPD-CO_2) was performed in the range of 40–500 °C under a He flow (10 °C min^{-1}, 16 ml min^{-1}). The samples were preheated under He flow (16 ml min^{-1}) at 700 °C for 1 h. Afterward, the temperature was decreased to 45 °C and the He flow was changed to pure CO_2 (16 ml min^{-1} for 0.5 h). The desorbed CO_2 was identified by an online thermal conductivity detector (TCD) after passing through a trap to remove any trace of water.

N_2 physisorption analysis was performed at a temperature of 77 K (−196 °C) on a gas adsorption analyzer ASAP 2020 physisorption/Micromeritics model in order to obtain the textural properties of the catalysts. Prior to analysis, the solids were degassed under vacuum at 200 °C for 2 h. From the obtained isotherms, the specific surface area (using the BET method), pore volume and pore diameter values were determined.

The morphology of the MCM-41 silica support and the dispersion of the cobalt ferrite were investigated by transmission electron microscopy (TEM) with an accelerating voltage of 120 kV (Jeol, JEM-2100, with EDS, Thermo scientific). The catalysts were prepared by placing one drop of the dispersion on a carbon coated copper grid (300 mesh).

2.4. Catalytic test

The ethylbenzene dehydrogenation reaction was performed in a fixed bed quartz microreactor using 60 mg of catalyst at 550 °C and atmospheric pressure under nitrogen flow (30 mL min^{-1}). Initially, for activating the oxide prior to the reaction, the material was pretreated under nitrogen flow (30 mL min^{-1}) for 60 min at 550 °C in order to remove water and physisorbed CO_2. Afterward, the ethylbenzene gas was brought into contact with the catalyst in the catalytic bed using a saturator containing ethylbenzene at 34 °C, which was carried by a N_2 and CO_2 mixture (30 mL min^{-1}), consequently leading to the dehydrogenation reaction. The CO_2 : ethylbenzene molar ratio was 30. Identification of the products and transformation of the reagent were analyzed by gas chromatography (GC, Clarus 680, Perkin Elmer) using an instrument equipped with a FID and a non-polar capillary column. *n*-Heptane was used as an internal standard for chromatographic analysis. The ethylbenzene conversion (C_{Et}) was calculated according to eqn (1), the product selectivity (S_{prod}) was calculated according to eqn (2) and the specific activity (A) was calculated according to eqn (3).

$$\%S_{\text{styrene}} = \frac{\text{Amount of obtained styrene (mol)}}{\text{Amount of all obtained products (mol)}} \times 100 \quad (2)$$

$$\%C_{\text{Et}} = \frac{\text{Amount of ethylbenzene consumed (mol)}}{\text{Amount of ethylbenzene introduced to the reactor (mol)}} \times 100 \quad (1)$$

$$A\left(\text{mol m}^{-2}\text{ h}^{-1}\right) = \frac{\text{Molar flow rate of ethylbenzene}\left(\text{mol h}^{-1}\right) \times C_{\text{Et}}}{\text{Catalyst mass (g)} \times \text{ surface area}\left(\text{m}^2\text{ g}^{-1}\right)} \quad (3)$$

2.5. Computational methods

In order to evaluate the exchange of iron with cobalt on the electronic structure of $CoFe_2O_4$ surfaces, DFT calculations were performed using periodic boundary conditions to better reproduce the two-dimensional surfaces. This allows evaluation of the ubiquitous long-range properties in the solid, which is more realistic and consistent with the obtained micrometric material.

To perform the theoretical approach, we have to consider that $CoFe_2O_4$ has a cubic structure (space group *Fd*3*m*), lattice parameter a = 8.35 Å and three non-equivalent atoms (1Co, 1Fe and 1O). The unit cell (atomic positions and lattice parameter) was fully optimized and the relaxed structure was used to model the low index (001) surface through the slab model, which is periodic in the x and y directions but finite in z. Slab (2 × 2) supercell expansion was employed to allow a better structural relaxation of the outermost surface layers. This slab contains 136 atoms, with a surface area of ~120 $Å^2$ and a thickness of ~8.4 Å. The (001) surface of several spinels has been used as a representative in many studies,[19,20] and it was concluded that the octahedral termination is more stable than the tetrahedral one. For an inverse spinel, the outer layers are undercoordinated octahedra [FeO_5], while the tetrahedral [CoO_4] are in the subsurface. Besides this configuration, two other possibilities were modeled in which one (12.5%) or four (50%) iron atoms on the octahedral sites were substituted by cobalt atoms, reaching a partially inverted spinel surface.

All theoretical DFT calculations were performed using the hybrid HHLYP functional[30] on the CRYSTAL 17 package,[31,32] also including the Grimme D3 dispersion correction to better describe long-range interactions.[33] The atomic centers were represented by an all-electron basis set: Co 8/6411/41 (s/sp/d), Fe 8/6411/41 (s/sp/d) and O 8/411/11 (s/sp/d), as available within the Crystal Basis Set Library.[34] The unrestricted Kohn–Sham formalism was adopted for all the systems to ensure the magnetic solution. The accuracy for the Coulomb and exchange series was controlled by five threshold parameters set to 8, 8, 8, 8, and 16. The shrinking factor (Pack–Monkhorst and Gilat net) was set to 6 for the bulk (or 2 for the slab supercell), corresponding to 16 (or 4) independent *k*-points in the irreducible part of the Brillouin zone integration. The SCF criteria convergence was governed by a threshold on the energy of 10^{-7} Hartree for geometry optimizations. All structures were optimized with the Broyden–Fletcher–Goldfarb–Shanno (BFGS) algorithm for Hessian updating, taking (0.0003 a.u.) for convergence criteria on the gradient and (0.00120 a.u.) for nuclear displacements.

The electronic structure was studied by means of atomic charges, electrostatic and charge density surfaces, band structure and density of states (DOS), analyzed using the properties 17 routine of the CRYSTAL code, considering the same setup used in the optimization, but improving the number of *k*-points to 20 during the diagonalization of the Fock matrix.

Electrostatic interactions have always been considered an important factor governing ligand–receptor and acid–base interactions from the catalytic point of view. The identification

of acidity and basicity sites of the spinel surfaces was done through electronic structure analysis, while the ability to adsorb the ethylbenzene molecule was predicted indirectly by means of an electrostatic potential, $V(r)$, complementary perspective, which is a descriptor for Lewis acidity.[35]

3. Results and discussion

3.1. Structural properties and chemical environment of iron/cobalt (XRD, Raman, Mössbauer and XPS)

The samples were analyzed by X-ray diffraction to study their crystalline properties. The results are presented in Fig. 1A. According to the literature, the formation of the α-Fe_2O_3 phase is expected for the sample Fe_2O_3–MCM-41, since the sample was calcined at a temperature of 700 °C after the impregnation process.[36] However, the Fe_2O_3–MCM-41 catalyst presented the profile of an amorphous phase without any diffraction peak. The amorphous material may be related to the formation of extremely small crystallites of α-Fe_2O_3 and/or a large number of defects (microstrain), which hinder their identification by XRD. The impregnation of Fe^{3+} on the MCM-41 surface leads to a high dispersion of the hematite phase, justifying the profile presented in the diffractogram. The XRD technique has a sensitivity limitation to identify phases with extremely small particle sizes. Earlier works on Fe_2O_3 dispersed on silica based supports showed the formation of Fe_2O_3 with crystallite sizes below the XRD detection limit (<4–6 nm).[21,37]

On the other hand, the sample CF-MCM-41 presented characteristic peaks of cobalt ferrite. Fig. 1A shows the experimental data and a column chart indicating the expected positions and intensities for the JCPDS 00–002-1045 card. The Rietveld refinement confirmed the formation of $CoFe_2O_4$ nanoparticles with a crystallite size of 8.6 nm. The experimental and theoretical diffractograms obtained from the refinement are detailed in the ESI, Fig. S1.†

The elemental analysis results obtained by XRF, Table S1,† show that the value of the Fe/Co mass ratio is close to that of cobalt ferrite. Furthermore, the mass ratio between Fe/Si and (Fe + Co)/Si is close to the values predicted in the synthesis

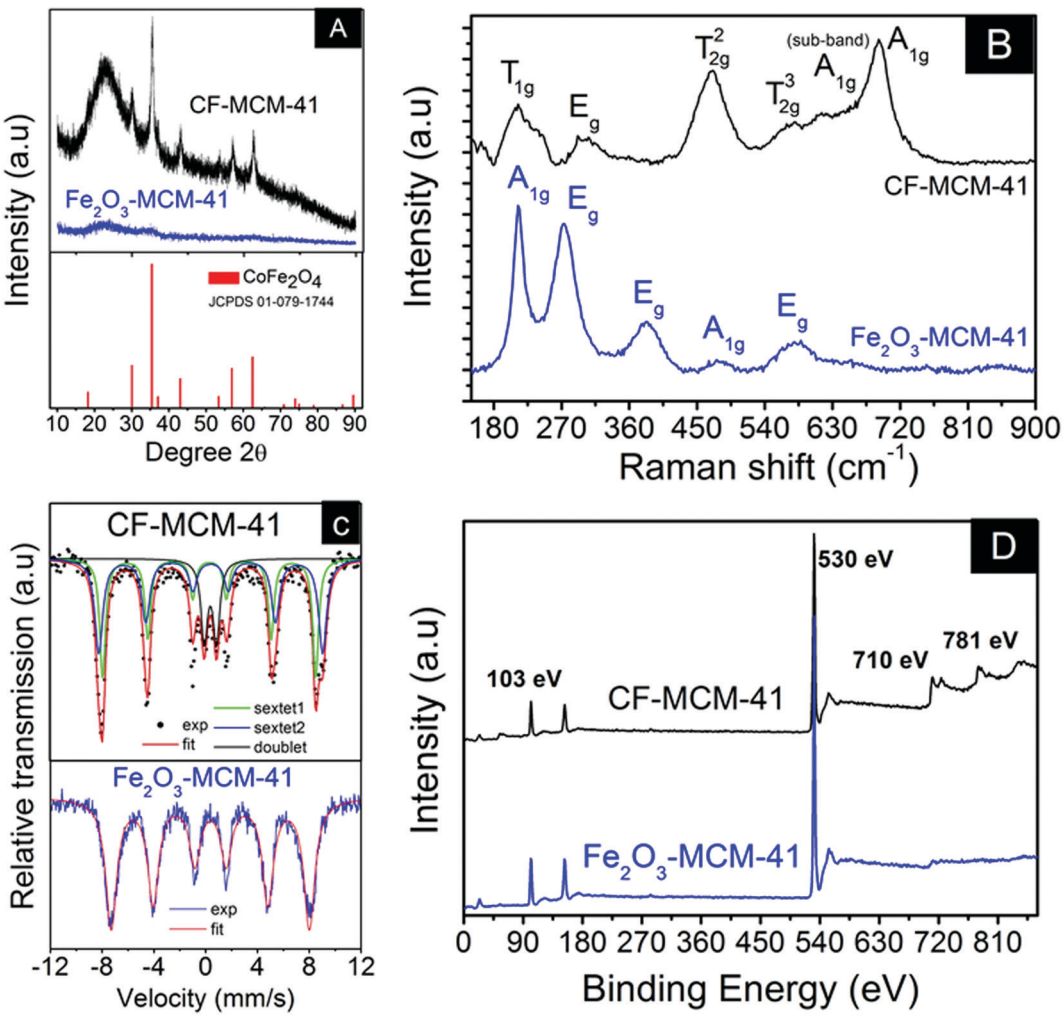

Fig. 1 Structural properties and chemical environment of Fe and Co for the different catalysts. (A) XRD results; (B) Raman spectra; (C) Mössbauer spectra at 12 K; (D) wide-scan XPS spectrum.

methodology, indicating that the ratio between the active site (Fe_2O_3 or $CoFe_2O_4$) and support (SiO_2–MCM-41) is similar for the two samples.

Low-angle XRD analyses were performed in order to study the change in the pore structure of MCM-41 after the impregnation process. The low-angle diffractograms are presented in the ESI, Fig. S2.† It is important to highlight that the pattern of ordered mesoporous MCM-41 shows a small number of reflections positioned at small angles due to the large lattice parameter. Generally, only three diffraction peaks are well resolved and are related to (100), (110), and (200) reflections.[38] These results confirmed the formation of the hexagonally ordered mesostructure of MCM-41.

Furthermore, some pores may be filled during the impregnation process, causing a slight change in the diffractograms.[39,40] Despite the slight difference in the diffractograms of the samples before and after impregnation, we can conclude that the MCM-41 structure was little affected. This result is important for catalytic application, allowing reagent accessibility to active sites and consequently the catalytic cycle.

Raman analyses were performed in order to obtain information about the formation of Fe_2O_3 and confirm the formation of $CoFe_2O_4$ for the CF-MCM-41 solid. The Raman spectra of both samples are presented in Fig. 1B. The spectra of Fe_2O_3–MCM-41 showed five typical bands of the α-Fe_2O_3 phase, located at 212 (A_{1g}), 272 (E_g), 384 (E_g), 477 (A_{1g}), and 582 cm^{-1} (E_g), originating from Raman active symmetric modes. A slight displacement of these bands compared to the values found in the literature was observed,[41,42] which may be related to structural defects such as oxygen vacancies and Fe^{3+} interstitials.[43] Thus, besides the small crystallite size, the presence of defects in the hematite structure may justify the absence of well-defined peaks in the diffractograms (Fig. 1A).

In Fig. 1B, the Raman spectra of the CF-MCM-41 catalyst has six Raman active modes for cobalt ferrite ($CoFe_2O_4$), $^3T_{2g}$ + E_g + $^2A_{1g}$. These six active modes are positioned at 210, 305, 470, 576, 618 and 690 cm^{-1}, which are in accordance with the spectra reported in the literature.[44–46] The well-defined band at 470 cm^{-1} (T_{2g}) is related to the oxygen–metal bond for metals in octahedral positions (Fe–O and Co–O). On the other hand, the band at 690 cm^{-1} is related to the oxygen–metal bonds for metals in the tetrahedral sites of the spinel structure. The band located at 618 cm^{-1} may also be correlated with the A1g mode (breathing of Fe–O and Co–O), designated as the A_{1g} sub-band, and is due to partial cation redistribution[42] and disorder effects of Co^{2+} and Fe^{3+} over the tetrahedral and octahedral sites.

Mössbauer spectroscopy was performed in order to obtain information about the chemical environment of Fe and to complement the information obtained from the XRD and Raman results. In addition, it is possible to extract information about the distribution of Fe^{3+} and Co^{2+} in the tetrahedral and octahedral sites, classifying the cobalt ferrite as a fully or partially inverted spinel. The analyses were carried out at room temperature and at 12 K, specifically for the Fe_2O_3–MCM-41 sample, in order to confirm the effect of crystallite size on XRD phase identification.

The room temperature spectrum obtained for the Fe_2O_3–MCM-41 catalyst (Fig. S3, ESI†) shows a central doublet indicating that, within the Mössbauer window time, the Fe_2O_3 nanoparticles are in the superparamagnetic regime. The superparamagnetic behavior is related to the small size of the nanoparticles and the temperature of measurement.[47] Thus, the Mössbauer spectrum confirms the results obtained from the XRD analysis, *i.e.* the absence of diffraction peaks regarding the Fe_2O_3 phase suggests (Fig. 1A) the formation of extremely small crystallites.

The low-temperature measurement shows a six-line Mössbauer spectrum (Fig. 1C). The spectrum is related to thermally blocked nanoparticles with slow relaxing magnetic moments, and confirms the superparamagnetic regime at 300 K. The hyperfine parameters of the spectra either at 12 or at 300 K show the presence of Fe^{3+} in the hematite structure. The isomer shift (IS) and hyperfine magnetic field (Hf) at 12 K are 0.365 mm s^{-1} and 48 T, respectively. These values are in close agreement with an earlier work in ultrasmall Fe_2O_3 nanoparticles.[48]

The Mössbauer spectrum of CF-MCM-41 at 12 K was fitted with two six-line spectra and one two-line spectrum. The sextets indicate the presence of Fe in two different environments in the thermally blocked nanoparticles, Fig. 1C. The doublet indicates the presence of superparamagnetic nanoparticles with very small sizes. The sextets are assigned to iron in the tetrahedral (Fe-Tetr, A site) and octahedral (Fe-Oct, B site) coordination symmetries. The hyperfine parameters presented in Table 1 are in close agreement with earlier results for $CoFe_2O_4$ and in accordance with previous characterized structures.[49,50]

The chemical formula of cobalt ferrites $(Co_{1-x}Fe_x)[Co_xFe_{2-x}]O_4$ can be obtained from the degree of inversion (x), which is defined as the fraction of Fe^{3+} occupying the tetrahedral sites. In the mentioned formula, cations enclosed in round and square brackets refer to ions in the A and B sites, respectively. The cobalt ferrite is fully inverted when $x = 1$. The degree of inversion can be calculated from the ratio of spectral relative absorption areas (RAA) given by the formula: $RAA(A\ site)/RAA(B\ site) = f_A/f_B(x/(2-x))$, where f_A/f_B is the ratio of recoilless fractions of Fe atoms in A and B sites. At low temperatures, it is known that $f_B/f_A = 0.96$,[50] thus, the chemical formula is given by: $(Co_{0.06}Fe_{0.94})[Co_{0.94}Fe_{1.06}]O_4$, where $x = 0.94$ indicates that the ferrite is partially inverted and a small fraction of Co^{2+} also occupies the tetrahedral positions.

XPS analyses were performed in order to consolidate the previous measurements with the chemical environment of Fe and Co on the solid surface, since the heterogeneous catalytic process occurs essentially on the surface. Wide-scan X-ray photoelectron spectroscopy (XPS) spectra are presented in Fig. 1D. The detailed spectra of Fe2p and Co2p for Fe_2O_3–MCM-41 and CF-MCM-41 samples are shown in the ESI, Fig. S4.†

The wide-scan XPS spectrum with binding energies ranging from 0 to 850 eV for the CF-MCM-41 solid shows four characteristic peaks at 103, 530, 710 and 781 eV related to Si

Table 1 Hyperfine parameters of the different samples containing iron before the catalytic test

Sample	Spectrum	IS (mm s^{-1})	QS (mm s^{-1})	B_{hf} (T)	Area (%)	Area – only $CoFe_2O_4$
CF-MCM-41	Sextet 1 (Fe_{tetr})	0.29	0.019	51	40	48
	Sextet 2 (Fe_{oct})	0.39	−0.011	54	45	52
	Doublet	0.36	0.9	—	15	—
Fe_2O_3–MCM-41	Sextet	0.36	−0.018	48	100	—

2p, O1s, Fe 2p and Co 2p, respectively. The wide scan XPS spectrum of the Fe_2O_3–MCM-41 solid shows photoelectron peaks at binding energies of about 103, 530, and 710 eV attributed to Si 2p, O1s, and Fe 2p, respectively. Si2p is related to the silicon oxide from the MCM-41 support. The wide-scan XPS spectra of the Fe_2O_3–MCM-41 and CF-MCM-41 samples are in agreement with previously published spectra.[51,52]

Fig. S4a† and B exhibit two XPS peaks at approximately 711 and 725 eV, which are identified as Fe^{3+}–O bonds in Co(II)Fe(III)$_2O_4$ oxide or α-Fe(III)$_2O_3$, corroborating with previous characterizations.[51,52] The Co 2p signal has four peaks at 781, 787, 797, and 803 eV, which confirmed the formation of the cobalt ferrite structure, Fig. S4c.† The Co $2p_{1/2}$ and Co $2p_{3/2}$ signals proved the Co^{2+} valence states. The two main peaks and the two satellite peaks confirmed the presence of Co^{2+} in the Co(II)Fe(III)$_2O_4$ structure, concerning the partially inverse spinel structures, indicating that the Fe and Co ions occupy both the tetrahedral and octahedral ferrite sites. The binding energy values observed in the spectra corroborate with previously published papers.[51,52]

The relative concentration of Co and Fe for the CF-MCM-41 catalyst has been calculated and found to be 48% and 52%, respectively, indicating that the Fe and Co present in the cobalt ferrite were equally distributed on the support surface. Prior to curve fitting, the background was subtracted and the peaks were deconvoluted. Furthermore, the superficial atomic concentrations of the different elements observed in the spectra in Fig. 1D are described in Table S1 (ESI†).

The experimental results shown above indicate that the impregnation method was successfully performed, since the ferrite structure for the CF-MCM-41 solid and the hematite phase for the Fe_2O_3–MCM-41 sample are present on the catalyst surface, which will be essential in the catalysis application.

The XRD, Raman, Mössbauer and XPS results presented essential information about the O^{-2}–Fe^{3+}–O^{2-} and O^{-2}–Co^{2+}–O^{2-} catalytic sites, which will be important in catalytic applications, since the Fe^{3+} and Co^{2+} (Lewis acid) and O^{2-}, lattice oxygen, (Lewis base) will have different electron densities and reactivities in the tetrahedral and octahedral sites.

3.2. Magnetic properties (VSM and M–T analysis)

Dormann *et al.*[48] studied finely dispersed hematite grains of 2.9 nm in an Al_2O_3 matrix. They found a sextet with an H_f of 47 T at 5 K and a two line spectrum at 300 K. Our spectrum, at 12 K, shows a sextet with a similar H_f to Dormann *et al.*[48] and with wide peaks indicating a distribution of H_f that can be ascribed to surface disorder; this effect is enhanced in small particles where the ratio of the surface to the core is relatively high. Therefore, our results are in close agreement with the work of Dormann *et al.*[48] and confirm the formation of very small hematite crystallites, which are in accordance with previously described characterizations.

The magnetization curves of Fe_2O_3–MCM-41 are presented in Fig. 2b. The isothermal measurement ($M \times H$) recorded at 300 K shows a non-saturated and very small magnetization signal at 50 kOe. The anhysteretic behavior of this measurement confirms the presence of fast relaxing magnetic moments due to superparamagnetic nanoparticles.

In fact, bulk hematite has a Néel transition (T_N) at 955 K. Also, it has a Morin transition (T_M) at 263 K and below this temperature the two magnetic sub-lattices are exactly antiparallel in the [111] axis. However, above T_M, the moments have a slight canting, therefore, resulting in a small net magnetization. It is known that T_M is below 4 K for particles smaller than 8 nm,[53] thus these particles will have a ferromagnetic signal above 4 K. The net magnetization in fine antiferromagnetic nanoparticles has contributions from the canting moments and from the uncompensated moments in the antiferromagnetic lattice.

The Mzfc curve shows a peak at 20 K due to the blocking temperature (T_B), Fig. 2a. On the other hand, the Mfc curve shows a steeper increase below T_B due to moments with enhanced magneto crystalline anisotropy, probably due to surface atoms. Furthermore, the Mzfc does not exhibit the Morin transition, indicating that the hematite nanoparticles may be smaller than 8 nm.[54] To further study the Fe_2O_3–MCM-41 sample, the hematite's particle size (D) was determined by assuming that they are spheres. The particle's volume (V) as a function of the blocking temperature (T_B), Boltzmann constant (K_B) and the magnetocrystalline anisotropy (K) is given by $V = 25K_BT_B/K$, where $V = \pi D^3/6$. Taking into account the K value determined by Dormann *et al.*[48] of $K = 9 \times 10^5$ J m^{-3} for very fine particles, we have obtained D = 2.5 nm, which is in close agreement with the work of Dormann *et al.*[48] and is reasonable for nanoparticles with sizes below the XRD detection limit, justifying the profile of the diffractogram for the Fe_2O_3–MCM-41 sample.

The hysteresis for the Fe_2O_3–MCM-41 sample shows that under a maximum magnetic field of 5 T the sample does not saturate at 4 K, Fig. 2b. The measurement shows a hysteresis with a coercive field of 1850 Oe and a magnetization at 5 T of 2.9 emu g^{-1}. This last value will be higher if we take into account the nominal concentration of hematite of 20 wt%, thus M(5 T) = 14.5 emu g^{-1}. The ferromagnetic signal suggests that

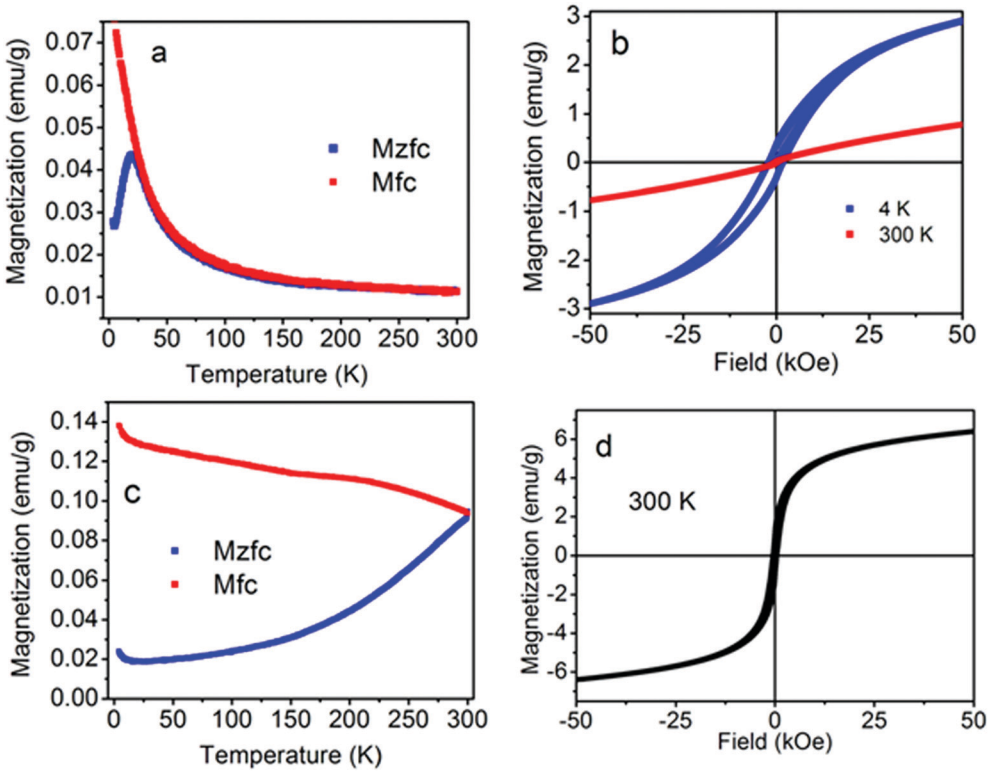

Fig. 2 Magnetic properties of the different samples. (a) and (c) Mzfc and Mfc magnetization curves; (b) and (d) hysteresis cycles from VSM analysis.

the Morin transition is below 4 K, therefore, the sample has canting moments, which contribute to the net magnetization.

For the CF-MCM-41 sample, the $M \times H$ measurement at 300 K shows an unusual behavior with a coercive field of 508 Oe, indicating that the sample is thermally blocked at 300 K, Fig. 2d. The magnetization at 5 T has a value of 6.45 emu g^{-1}. This value is smaller than the one expected for the bulk inverse spinel cobalt ferrite of 72 emu g^{-1}. However, for the present catalyst, the active phase has a small crystallite size and is dispersed in the MCM-41 support, which justifies the lower value of saturation magnetization presented in the hysteresis curve, Fig. 2d. The Mzfc and Mfc curves do not show any peak in the whole range of temperatures, Fig. 2c. These results confirm that the sample is thermally blocked below 300 K, Fig. 2d. It is known that cobalt ferrite nanoparticles with sizes larger than 6 nm are blocked at 300 K,[53] which is in agreement with the crystallite size of 14 nm, calculated using Scherrer's equation. Catalysts with magnetic properties are interesting, since they are easily separated at the end of the process by simple magnetic extraction.

3.3. Redox properties of cobalt ferrite (TPR-H_2 analysis)

The TPR analysis was performed to study the redox properties of Fe^{3+} and Co^{2+} in the tetrahedral and octahedral sites of the spinel structure. Fig. 3 presents the TPR profile for the two samples. The Fe_2O_3–MCM41 solid showed one well-defined peak at low temperature and two shoulders at higher temperatures. The broad peak with a maximum near 405 °C is related to the transformation of hematite to magnetite. The two shoulders at approximately 530 and 580 °C, respectively, may be related to the reduction of magnetite (Fe_3O_4) to FeO followed by reduction of FeO to metallic iron. The reduction of a fraction of magnetite to metallic iron with lower support interaction and located on the external surfaces may have occurred in the first reduction range, since the amount of H_2 consumption in the first peak is much greater than those in both shoulders at higher temperatures, indicating the incomplete reduction of Fe^{2+} at higher temperatures. Thus, the two shoulders may be related to the reduction of the iron oxide that is more protected by the support and therefore H_2 has limited access, complicating the reduction process. These observations are in agreement with other previously published papers.[55,56]

On the other hand, it is noted from the TPR profile for the CF-MCM-41 sample that Fe^{3+} ions located in the tetrahedral and octahedral positions of the ferrite structure have different redox properties compared to the Fe^{3+} ions present in the hematite structure, considering that the heterogeneity of the spinel structure is much higher. Specifically for this sample, two broad and low-intensity shoulders are observed at low temperature and three well-defined peaks at higher temperature. These peaks must be related to the reduction of the divalent cation ($Co^{2+} \rightarrow Co^{+} \rightarrow Co^{0}$) and the trivalent cation ($Fe^{3+} \rightarrow Fe^{2+} \rightarrow Fe^{0}$) in the tetrahedral and octahedral positions of the cobalt ferrite structure. Taking into account that

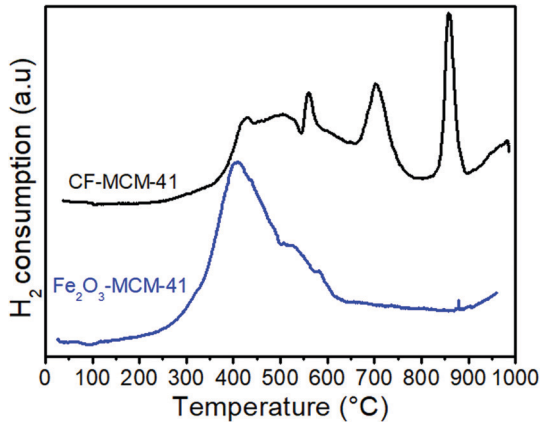

Fig. 3 H_2-TPR results for the different solids.

in the crystallites the octahedral sites are more exposed compared to the tetrahedral sites, one may consider that the reduction of the octahedral sites occurs preferentially (greater reactivity) compared to that of the tetrahedral sites.[57,58] The literature reports that in the TPR curve the Co^{2+} reduction cannot be easily differentiated from the Fe^{3+} reduction, since both occur in the same temperature range. In addition, the presence of Co^{2+} (more easily reduced cation) shifts to lower temperatures the traditional reduction range of Fe^{3+}, justifying the similar reduction temperature range.[59]

Many studies report that the reduction of Co^{2+} and Fe^{3+} to zero valent metals does not completely occur in the permitted temperature range for H_2-TPR analyses,[54,55] indicating that the ferrite spinel has high structural stability against a reducing atmosphere. Furthermore, the structural stability of Fe^{3+} in $CoFe_2O_4$ against a reducing atmosphere is much larger than that of Fe^{3+} in α-Fe_2O_3, which is confirmed in our TPR results where the CF-MCM-41 catalyst showed reduction peaks at a higher temperature compared to the Fe_2O_3–MCM-41 sample. For oxidative dehydrogenation of hydrocarbons where Fe^{3+} plays an important role, the cobalt ferrite catalyst will probably have a better performance compared to the hematite because the ferrite will have greater structural stability and will minimize the deactivation due to the reduction of Fe^{3+} during the catalytic dehydrogenation cycle.[60,61]

3.4. Acidity and adsorption properties of NO (IR of adsorbed pyridine and NO)

The IR spectra of pyridine adsorbed on Fe_2O_3–MCM-41 and CF-MCM-41 catalysts are presented in Fig. 4a. The most intense bands appear at approximately 1449, 1490 and 1608 cm^{-1} and are related to Lewis acidic sites, referring to Fe^{3+} present in the hematite and Fe^{3+}/Co^{2+} present in the cobalt ferrite. The bands at 1490 and 1608 cm^{-1} are absent in pure MCM-41, indicating that the Lewis acid sites are mostly from the hematite and cobalt ferrite structure. Previous studies have shown that, for the case of the CF-MCM-41 solid, the band at 1609 cm^{-1}, the contribution of pyridine adsorption in octahedral sites is greater than that in the tetrahedral positions, suggesting that the octahedral sites are mostly exposed on the catalyst surface compared to the tetrahedral sites.[15,62] Specifically, for the pure MCM-41 support, the spectrum exhibits two visible bands at 1446 and 1597 cm^{-1}, which are associated with the adsorption of pyridine on the free silanol groups present in the MCM-41 structure, since pyridine forms hydrogen bonds with silanol groups.[63]

Adsorption of NO followed by infrared analysis was performed in order to evaluate the adsorption capacity of NO in Fe^{3+} and Co^{2+} sites, obtaining information about the surface chemistry of Lewis acid sites. The NO species presents three electron pairs occupying bonding orbitals and one unpaired electron situated on a π antibonding orbital. In addition, another electron pair is positioned on the 5σ nonbonding orbital. These characteristics make NO a weak electron donor (a weak Lewis base), presenting the ability to coordinate with Lewis acid sites such as Co^{2+} and Fe^{3+}.[64]

The IR spectra of NO adsorbed on Fe_2O_3–MCM-41 and CF-MCM-41 solids are shown in Fig. 4b. The results clearly show that the bands are much more intense in the CF-MCM-41 sample compared to those in the Fe_2O_3–MCM-41 catalyst, suggesting that the active area referring to the Lewis acid sites is much more exposed in the cobalt ferrite compared to that in the hematite. The NO adsorption on the surfaces containing Fe^{3+} or Fe^{3+}/Co^{2+} sites may be attributed to two types of interactions, designated as monodentate and bidentate nitrates. The adsorption of NO on the MCM-41 support practically does not exist, since the spectrum of the pure support did not show any visible band.

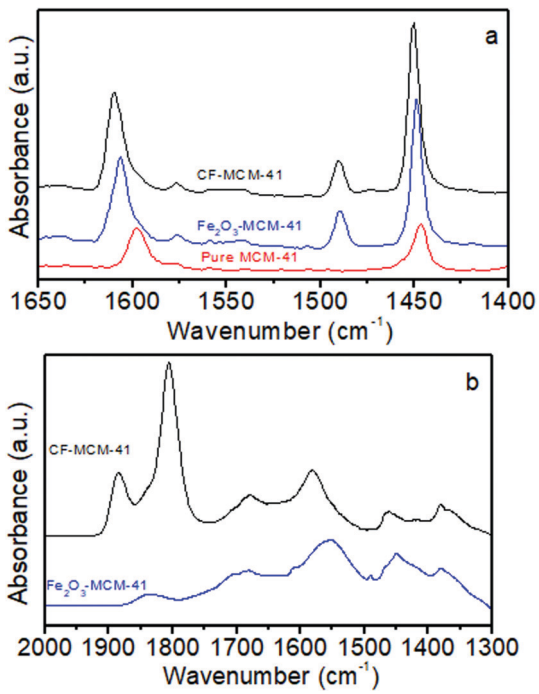

Fig. 4 Chemical adsorption followed by infrared analysis. (a) FTIR spectra of pyridine adsorbed on the solid surface; (b) FTIR spectra of NO adsorbed on the catalyst surface.

The CF-MCM-41 catalyst exhibited six bands at approximately 1382, 1463, 1582, 1681, 1806, and 1885 cm^{-1}, respectively. The Fe_2O_3–MCM-41 solid showed three visible bands at 1380, 1451 and 1555 cm^{-1} (similar to CF-MCM-41) and two very weak bands at 1681 and 1836 cm^{-1}. The bands at 1806 and 1885 cm^{-1} belong to the cobalt ferrite and may be related to ν_s(NO) and ν_{ass}(NO) modes due to the formation of $Co^{2+}(NO)_2$ or $Fe^{3+}(NO)_3$ complexes.[65,66] The bands at approximately 1382 and 1450–1463 cm^{-1} may be assigned to monodentate nitrate species, while the bands at approximately 1555–1582 and 1681 cm^{-1} are attributed to bidentate nitrate species.[67]

Specifically for the CF-MCM-41 sample, the NO species can be adsorbed in the Fe^{3+} or Co^{2+} sites and in the tetrahedral or octahedral positions of the lattice. Computational studies using the DFT approach have shown that the NO molecule is preferentially adsorbed by Fe^{3+} compared to divalent ions and preferably adsorbed in the octahedral positions compared to the tetrahedral positions in the crystal lattice of the ferrite structure.[68,69] Thus, the Fe^{3+} ions located in the octahedral positions will be possibly the preferred sites in the cobalt ferrite for reactions where the Lewis acid sites play an important role in the catalytic cycle.

3.5. CO_2 adsorption capacity and catalyst basicity (TPD-CO_2)

CO_2 desorption analysis was performed in order to evaluate the CO_2 adsorption capacity considering that CO_2 plays the role of a soft oxidant during oxidative ethylbenzene dehydrogenation, minimizing coke deposition. The TPD-CO_2 results are presented in Fig. 5. All the catalysts show a main peak at low temperature between 27 and 190 °C. Particularly, the Fe_2O_3–MCM41 solid showed a broad and low intensity band between 150 and 275 °C. The first CO_2 desorption peak observed in both samples is related to monodentate carbonate formed on weak basic sites. The Fe_2O_3–MCM-41 catalyst showed greater heterogeneity of the weak basic sites since one shoulder was observed at 97 °C, while the CF-MCM-41 sample, despite the greater homogeneity, presented a higher number of weak basic sites due to the greater area of the band at low temperature. The Fe_2O_3–MCM-41 solid has a broad and low-intensity band with two shoulders at 192 and 240 °C; these signals are related to CO_2 desorption of bidentate carbonate formed on moderate basic sites. It is worth mentioning that CO_2 adsorbed in the bidentate form (moderate sites), for some reactions, is considered as an occupant of the active sites hindering the catalytic cycle, while in the monodentate form (weak sites) it is easily desorbed, releasing the active site to the new catalytic cycle.[70,71] Thus, it is expected that for higher amounts of CO_2 adsorbed on the catalyst surface, especially in weak sites, the activity in oxidative dehydrogenation will be greater due to the lower amount of deposited coke (less obstruction of active sites by carbon).

3.6. Textural properties (N_2 adsorption–desorption isotherms)

The nitrogen physisorption isotherms are presented in Fig. 6. The corresponding calculated parameters are listed in

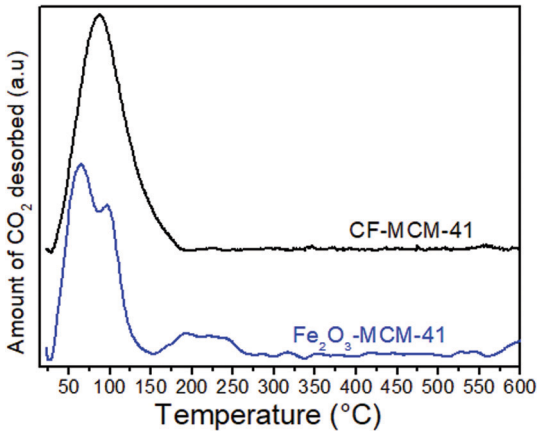

Fig. 5 CO_2 desorption curves for the different solids (TPD-CO_2).

Table 2 (surface area, pore volume and pore diameter). All the samples exhibited a type IV isotherm according to IUPAC classification with a sharp capillary condensation step at about 0.25 and 0.6 relative pressures, characteristic of mesoporous silica MCM-41 based materials.[72] The range of pore size distribution was very narrow, indicating the uniformity of pores and preservation of mesoporosity. The data referring to the textural properties present in Table 2 indicate that the surface area decreased after Fe^{3+} and Co^{2+} impregnation. The pore volume also had a slight decrease after insertion of the metals by incipient impregnation. These results suggest that the metals inserted by impregnation are mostly on the catalyst surface, as presented in the XPS results (Fig. 1D), and a small fraction of pores is partly blocked by the hematite (Fe_2O_3–MCM-41 sample) or cobalt ferrite (CF-MCM-41 solid). Despite the slight change in texture properties after impregnation, the mesoporous structure of the MCM-41 support was practically maintained, corroborating with the low-angle diffractograms (Fig. S2†).

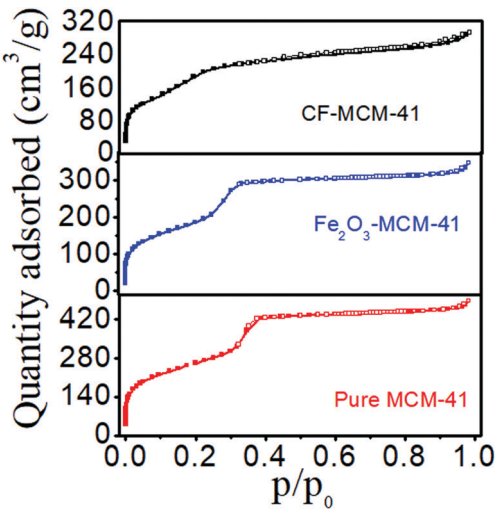

Fig. 6 N_2 adsorption and desorption isotherms for the different samples.

Table 2 Textural properties obtained from N_2 adsorption–desorption isotherms and specific activity from catalytic performance (A)

Sample	S_{BET} ($m^2\ g^{-1}$)	V_p ($cm^3\ g^{-1}$)	D_p (nm)	$A^{\#}$ (mol $m^{-2}\ h^{-1}$)
Pure MCM-41	946	0.75	4.2	0.03
Fe_2O_3–MCM-41	690	0.53	3.9	0.05
CF-MCM-41	789	0.45	3.4	0.23

S_{BET}: BET surface area; V_p: total pore volume; D_p: pore diameter obtained by the VBS, method.; # = average values only for a reaction period higher than 2 h.

3.7. Morphological properties (TEM images)

TEM characterization was employed in order to observe the mesoporous structures of the CF-MCM-41 solid. TEM images of the CF-MCM-41 catalyst are presented in Fig. 7.

Fig. 7A shows a particle with well-defined long fringes related to pores of the MCM-41 particle with inter pore distances of 3.3 nm in agreement with the small-angle XRD diffractograms (Fig. S2†) and N_2 isotherms (Fig. 6). In the lower right side, there are a large number of aggregates of small particles, probably due to CF, deposited on the MCM-41 surface. Fig. 7B shows the same particle recorded at a lower magnification; in the upper side of the MCM-41 particle, a large number of small nanoparticles that seem to clog the MCM-41 pores are noticed. Approximately, the particle in Fig. 7B is 200 nm wide and has a length of 300 nm. Fig. 7C shows a high magnification image with a few CF nanoparticles depicting fringes due to (400) and (311) planes with interplanar distances of 0.20 nm and 0.25 nm, respectively, according to the JCPDS 00–002-1045 card shown in the diffractograms in Fig. 1A. Fig. 7D shows a histogram with the size distribution of the CF particles, and the main size is about 7 nm, which is in agreement with the value obtained from the diffractograms according to the Scherrer equation.

3.8. Catalytic performance (catalytic tests)

The catalytic performance of the different samples in the ethylbenzene conversion to styrene is shown in Fig. 8. The results indicate that pure MCM-41 support has practically no activity in the reaction with a conversion value close to 3% (practically inactive), confirming that the O^{-2}–Fe^{3+}–O^{2-} and/or ^{-2}O–Co^{2+}–O^{2-} species in the crystal lattice are the major sites responsible for the conversion of ethylbenzene to styrene. The CF-MCM-41 catalyst exhibited better conversion results compared to the Fe_2O_3–MCM-41 solid, confirming that the cobalt ferrite is a more stable structure for the reaction conditions compared to the hematite. The $CoFe_2O_4$ structure minimizes the deactivation by reduction of the active sites and by coke deposition compared to the α-Fe_2O_3 phase.

The diffractogram of the CF-MCM-41 sample after the catalytic test, Fig. S5,† confirms the high stability of the cobalt ferrite structure compared to the hematite, since practically no difference was observed compared to the diffractogram before the reaction (Fig. 1A). The Mössbauer spectroscopy results after the reaction (not shown) also confirmed the presence of cobalt ferrite. The identification of the hematite phase change to magnetite for the Fe_2O_3–MCM-41 sample after the reaction was not possible, since this sample has a crystallite size below the XRD

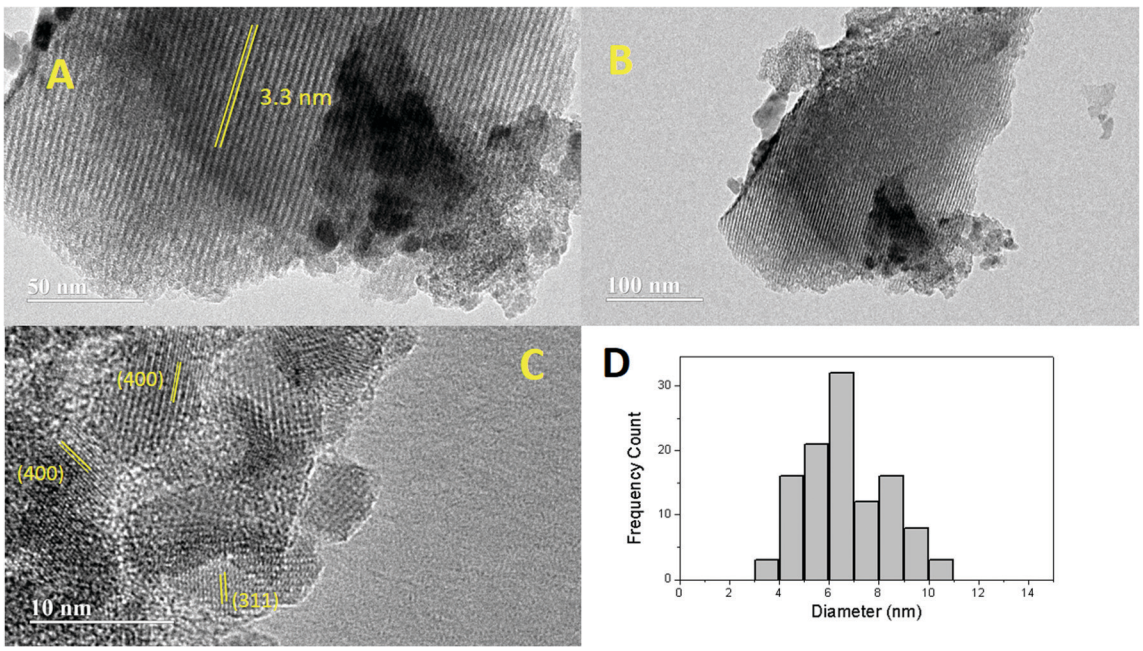

Fig. 7 (A)–(C): TEM images of the CF-MCM-41 catalyst using different approximations. (D): Histogram with the size distribution.

detection limit as mentioned previously. On the other hand, it was previously described from the experimental data after and before the reaction that for catalysts containing hematite dispersed in a silica support a change of hematite to magnetite occurs,[16,21] justifying the better catalytic performance of the cobalt ferrite compared to the hematite. It is known that the catalytic performance for the oxidative dehydrogenation of ethylbenzene using magnetite (Fe^{3+}/Fe^{2+}) is smaller compared to that using hematite (Fe^{3+}),[73] confirming that the restitution of Fe^{3+} sites during the catalytic cycle is essential for maintaining the catalyst activity.

The CF-MCM-41 sample reached ethylbenzene conversion values around 30% after 60 min of reaction and remained constant during the 300 min reaction, while the Fe_2O_3–MCM-41 solid was deactivated during the reaction, presenting ethylbenzene conversion values close to those of the support in the last minutes of reaction. Both samples presented almost 100% selectivity to styrene, confirming that iron-based materials are highly selective to styrene. Traces of benzene and toluene were identified in some reaction time. The results of specific activity presented in Table 2 confirm the higher conversion of the sample containing cobalt ferrite compared to hematite and the pure support.

3.9. Mechanistic proposal (catalytic cycle)

The reaction mechanism may change according to the nature of a solid catalyst. The materials need certain characteristics such as active sites well distributed on the surface; the accessibility of the sites in relation to the reagents is affected by physicochemical properties (elemental composition, structure, oxidation states, crystallite size, morphology, texture, acidity–basicity and dispersion of active sites).[74] All characterizations and catalytic tests presented previously confirmed that the cobalt ferrite has interesting properties to act as a catalyst in the transformation of ethylbenzene to styrene, since this structure presents Fe^{3+} (major active site) with a high stability structure. However, the role of iron or cobalt and lattice oxygen sites in the tetrahedral or octahedral positions of the cobalt ferrite in the transformation of ethylbenzene to styrene needs to be clarified.

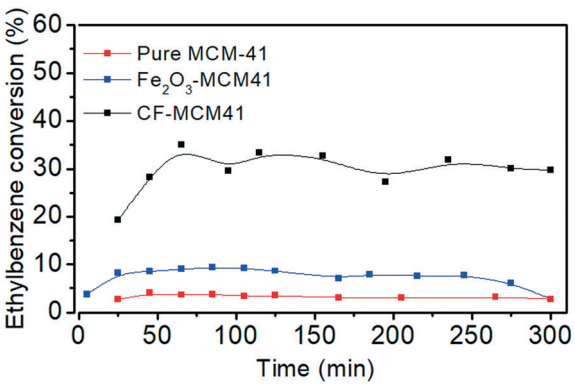

Fig. 8 Catalytic performance of the cobalt ferrite in the oxidative dehydrogenation of ethylbenzene.

The mechanism for oxidative dehydrogenation of hydrocarbons using an iron oxide-based catalyst (Fe^{3+} sites) has been previously discussed in the literature.[75,76] Initially the adsorption of the hydrocarbon group interacting with the Fe^{3+} active site and O^{2-} (lattice oxygen) occurs, followed by desorption steps, releasing H_2 and the hydrocarbon product), and finally the reoxidation step, regenerating the solid. The sequence of reactions relating to this mechanism is presented below. Oxidative dehydrogenation of ethylbenzene occurs in two steps. Initially, simple dehydrogenation occurs, producing styrene and H_2, reaction (4). Subsequently, the generated H_2 reacts with CO_2 to produce $H_2O(g)$ and $CO(g)$ through the reverse water-gas shift section (RWGS), reaction (5).

$$C_6H_5 - CH_2CH_3(g) \rightleftharpoons C_6H_5 - CH = CH_2(g) + H_2(g) \quad (4)$$

$$CO_2(g) + H_2(g) \rightleftharpoons CO(g) + H_2O(g) \quad (5)$$

$$C + CO_2(g) \rightarrow 2CO(g) \quad (6)$$

$$Fe^{3+}\text{ (present in crystalline structure)} \rightarrow Fe^{2+} \quad (7)$$

$$Fe^{2+} \rightarrow Fe^{3+}\text{ (present in crystalline structure)} \quad (8)$$

Particularly, some studies have reported the hydrocarbon dehydrogenation mechanism using ferrite catalysts. In this case, hydrogen abstraction occurs in two steps. In the first step, a homolytic cleavage occurs to produce the intermediate by forming a π bond with the Fe^{3+} sites. During the second step, a heterolytic cleavage occurs, in which H^+ binds to the O^{2-} species (lattice oxygen sites) and forms a C_xH_y–Fe^{3+} complex, reactions (7) and (8). The abstraction of α hydrogen is significantly influenced by the acidic properties of the catalyst.[77] Although some works proposed a mechanism for oxidative dehydrogenation of hydrocarbons using ferrites, the action of these sites and their role in the oxidative dehydrogenation of ethylbenzene remains a challenge to be explored. Furthermore, previous studies did not mention the action of tetrahedral and octahedral sites of ferrites. Thus, Scheme 1 shows a mechanistic proposal for the oxidative dehydrogenation of ethylbenzene to styrene using the $CoFe_2O_4$ catalyst.

The reaction begins when the Fe^{3+} sites (Lewis acids) in the Co(II)Fe_2(III)O_4 structure adsorb the aromatic ring of ethylbenzene (step I), followed by the elimination of two hydrogen from ethyl groups over Lewis basic centers (O^{2-}), lattice oxygen, with electron transfer to Fe^{3+} (step II). In this stage of the mechanism, the C–H bond is broken. Joseph *et al.* proposed that the basic aromatic molecule adsorbed in the Lewis acid sites of iron maintains an interaction with the highest occupied molecular orbital (HOMO) and the unoccupied states of the 3d iron have to be assumed (LUMO).[78] In step (III), iron and oxygen were reduced according to Lewis acid/base interactions. Considering the desorption of the H^+ ions from the basic center (O^-) and the interaction of the

acid center (Fe^{2+}) with styrene, the reaction will produce H_2 and styrene (reaction (4)).

The reduction of iron, reaction (7), and formation of OH groups during the reaction and desorption represents a stage of catalyst deactivation. Thus, new reactions are trivial to restore the Fe^{3+} active sites and reestablish the catalytic cycle. The reoxidation of the iron active sites occurs in step (IV), reaction (8), returning to the initial state and consequently continuing the cyclic mechanism. For this stage, the literature proposes some mechanisms,[79] such as homolytic cleavage of the OH group, producing H_2. In experimental studies, Zhang *et al.*[80] pointed out that the water-gas reverse reaction occurs during dehydrogenation with CO_2 and facilitates ethylbenzene conversion. The presence of CO_2 helps to sustain the ethylbenzene dehydrogenation in the $CoFe_2O_4$ structure, removing the hydrogen and repairing the oxygen vacancy created on the ferrite surface.

The Fe^{3+} ions (tetrahedral and octahedral sites) present in the ferrite are the main acid sites responsible for attracting the aromatic ring because they have a higher Lewis acid strength compared to Co^{2+} in the ferrite structure located in the tetrahedral and octahedral sites. In addition, the octahedral sites are predominant compared to the tetrahedral sites, since they are more abundant in the cobalt ferrite surface.[81] Therefore, the lattice oxygen in the vicinity of the Fe^{3+} in the octahedral position plays the role of abstracting the hydrogens from ethylbenzene and dehydrogenates with greater intensity compared to the lattice oxygen (basic site) near Co^{2+} in the tetrahedral and octahedral positions.

On the other hand, the catalytic dehydrogenation cycle performed by the $^{-2}O–Co^{2+}–O^{2-}$ sites in the tetrahedral and octahedral positions cannot be neglected, since some studies have reported that oxidative dehydrogenation of hydrocarbons occurs in the presence of Co_3O_4-based catalysts.[82,83] Tyo *et al.* described the oxidative dehydrogenation in the presence of cobalt oxide from experimental and theoretical studies.[83] The activation of hydrocarbon bonds occurs by heterolytic or homolytic mechanisms involving pairs of metal–oxygen (M–O*) or oxygen–oxygen (O*–O*) sites, similar to previously described mechanisms. The heterolytic dissociation occurs through the σ bond, involving the oxidative addition of C–H together with an abstraction of a proton by the basic site (O*) on the surface. The C–H homolytic activation involves the abstraction of hydrogen where a basic oxygen atom on the surface abstracts an H˙ and results in a weakly coordinated species designated as C_3H_7 (˙). The C_3H_7 readily returns to a second oxygen in the surface during the course of the reaction. The reaction occurs on two surface oxygen atoms (O*–O*), providing the dehydrogenation process.

In spite of the evidence presented for the preferential adsorption of Fe^{3+} compared to Co^{2+} and the preferences for the octahedral sites compared to the tetrahedral sites in the ferrite structure, no study using the DFT approach has been presented for ethylbenzene adsorption to confirm this assumption. Hence, a DFT computational study of ethylbenzene adsorption on the $CoFe_2O_4$ surface was carried out in order to understand the site preference for adsorption of ethylbenzene and confirm the mechanism proposed in Scheme 1.

3.10. Computational study (DFT)

Fig. 9A shows the optimized $CoFe_2O_4$ bulk, where the lattice parameter (a = 8.31 Å) was in close agreement with

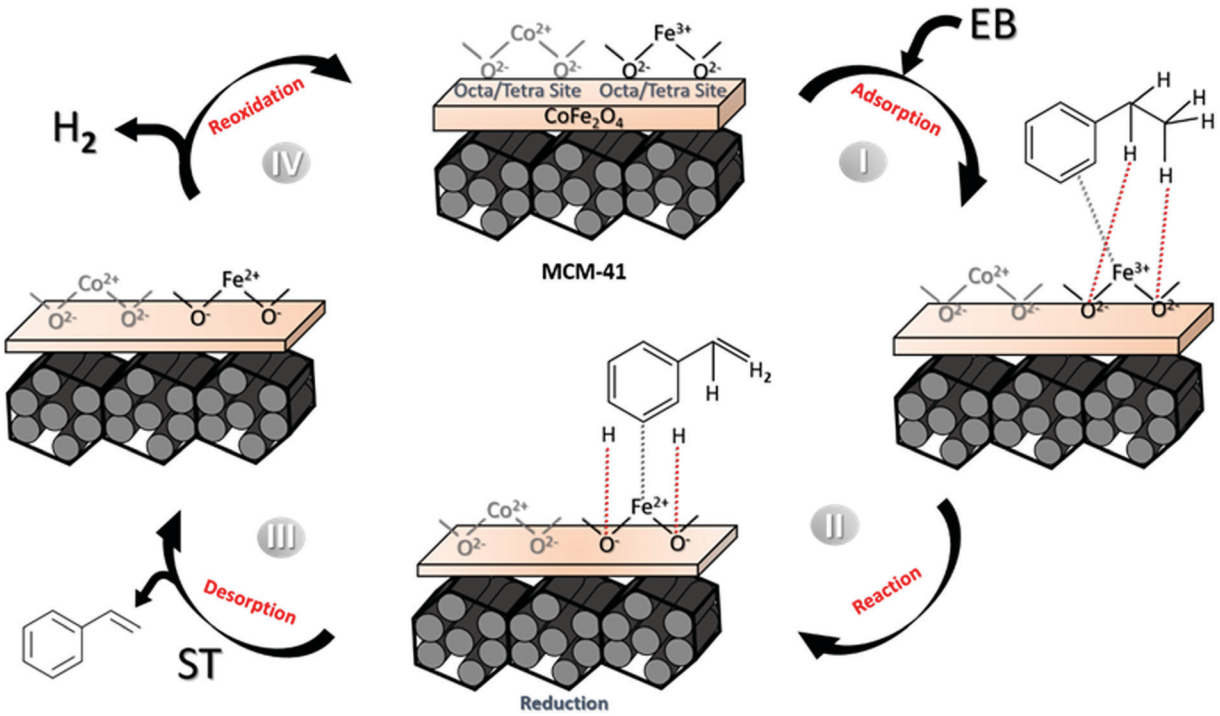

Scheme 1 Scheme indicating the mechanistic proposal for the oxidative dehydrogenation of ethylbenzene using catalysts based on cobalt ferrite.

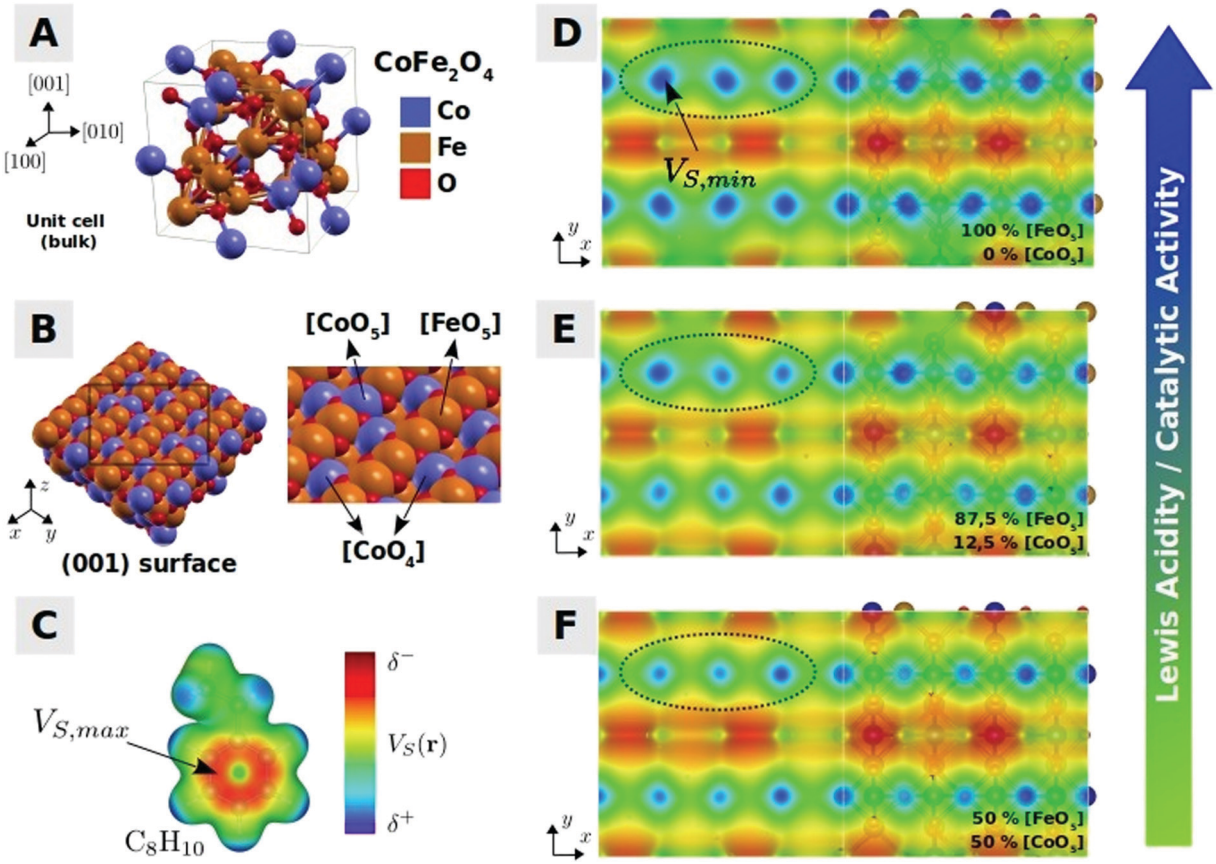

Fig. 9 (A) Unit cell of cubic $CoFe_2O_4$. (B) (001) surface where the octahedral and tetrahedral sites at the outermost layers are occupied by Co or Fe. The electrostatic surface potential [*VS*(*r*)] for (C) ethylbenzene (0.01 a.u. isodensity) and (D–F) the top view of spinel (001) termination (0.001 a. u. isodensity).

experimental results, Fig. 1A. This bulk was used to build the surfaces in the (001) plane, Fig. 9B, in which the octahedral sites are occupied by iron or cobalt with a five-fold coordination [MO_5]. The nature of site occupation and its coordination are determinant for the adsorptive power of a surface. For adsorption of aromatic compounds, for example, the surface should have a Lewis acid character to be able to interact through π-bonding of the ring with the undercoordinated transition metal at the surface. In fact, as previously described, the benzene molecule interacts preferentially with the hematite (001) surfaces through π-bonding in parallel geometries, and only weakly through hydrogen bonds in vertical geometries.[78] By visual inspection of the electrostatic potential surface of ethylbenzene (Fig. 9C) and the catalyst (Fig. 9D–F), it is easy to infer that ethylbenzene interacts with the surface of $CoFe_2O_4$ in a similar way to C_6H_6/Fe_2O_3 as described by Dzade *et al.*[84]

The change in the Fe/Co amount in the (001) surfaces affected locally the adsorption site acidity, as depicted in Fig. 9D–F, by the modulation of $V_{S,\min}$. In general, the effect of the cobalt increase on the surface leads to a decrease in positive electrostatic potential, which indicates that the adsorption capacity of ethylbenzene should become preferential in iron. Another important factor for ethylbenzene dehydrogenation into styrene is the role of C–H···O_2– interaction, which takes place in the $V_{S,\max}$ region of surfaces (red areas in Fig. 9D–F, which are the sites most prone to interact as Lewis bases). Moreover, the main product of ethylbenzene dehydrogenation, styrene, has a π-conjugated (–CH=CH_2) vinyl group that decrease the basicity of the aromatic ring, favoring the desorption of the reaction product and consequently the catalytic cycle. Thus, the DFT results showed good agreement with the mechanism proposed in Scheme 1.

The electronic effect of the Fe/Co ratio on (001) surfaces is also observed by density of states (DOSS) analysis (Fig. S6, ESI†), where the pristine cobalt ferrite has the edge of the valence band (VB) composed mainly of partially filled Fe 3d states, while the bottom of the conduction band (CB) was composed of Co 3d states. A similar behavior was observed when few octahedral sites are inverted (12.5% [CoO_5] and 87.5% [FeO_5]), but it was not observed when the amount of cobalt was increased on the surface, where an empty Co 3d midgap state was created, reducing the band gap.

4. Conclusions

Catalysts based on cobalt ferrite dispersed on MCM-41 were successfully synthesized and applied in the conversion of

ethylbenzene to styrene. The active sites in the cobalt ferrite structure are more promising for the transformation of ethylbenzene to styrene compared to the traditional sites present in the hematite structure. A partially inverted Co ferrite was obtained with the chemical structure $(Co_{0.06}Fe_{0.94})[Co_{0.94}Fe_{1.06}]O_4$, where Co^{2+} and Fe^{3+} occupy both octahedral and tetrahedral positions. Catalytic tests showed excellent selectivity and stability for the $CoFe_2O_4$ phase, which are attributed to high structural stability against the reaction conditions compared to the hematite (low structural stability). The mechanistic proposal has shown that ethylbenzene mainly prefers the Fe^{3+} sites compared to Co^{2+} and the dehydrogenation occurs preferentially in the octahedral sites compared to the tetrahedral sites. The computational study using DFT confirmed that the catalytic process for ethylbenzene dehydrogenation occurs preferentially in iron and lattice oxygen sites located in the octahedral positions, but the cobalt sites and the tetrahedral positions in the cobalt ferrite structure cannot be completely neglected.

Conflicts of interest

There are no conflicts to declare.

Acknowledgements

The authors would like to thank the Brazilian CNPq and CAPES funding agencies for financial support. We also thank Tatiane Oliveira at LABMIC-UFG for providing the TEM images, Professor José Marcos Sasaki for XRF analysis and Professor Jhonny Villarroel for assisting in the interpretation of N_2 physisorption analysis. The computational facilities were supported by resources supplied by Brazilian Funding Agencies FAPESP, CNPq and the Center for Scientific Computing of the São Paulo State University (Grid Unesp).

References

1 S. G. Sanz, L. McMillan, J. McGregor, J. A. Zeitler, N. Al-Yassir, S. Al-Khattaf and L. F. Gladden, *Catal. Sci. Technol.*, 2015, **5**, 3782.
2 Z. Z. Wu, N. C. Nelson, A. D. Sadow, I. I. Slowing and S. H. Overbury, *ACS Catal.*, 2015, **5**, 6426–6435.
3 A. Schüle, O. Shekhah, W. Ranke, R. Schlögl and G. Kolios, *J. Catal.*, 2005, **231**, 172–180.
4 T. P. Braga, E. Longhinotti, A. N. Pinheiro and A. Valentini, *Appl. Catal., A*, 2009, **362**, 139–146.
5 M. de S. Ramos, M. de S. Santos, L. P. Gomes, A. Albornoz and M. do C. Rangel, *Appl. Catal., A*, 2008, **341**, 12–17.
6 C. Wang, J. Shi, X. Cui, J. Zhang, C. Zhang and L. Wang, *J. Catal.*, 2017, **345**, 104–112.
7 T. P. Braga, A. N. Pinheiro, C. V. Teixeira and A. Valentini, *Appl. Catal., A*, 2009, **366**, 193–200.
8 X. Li, J. Feng, H. Fan, Q. Wang and W. Li, *Catal. Commun.*, 2015, **59**, 104–107.
9 V. R. Madduluri, P. Nagaiah, C. Prathap, K. Vasikerappa, A. Nagu, B. D. Raju and K. S. R. Rao, *Arabian J. Chem.*, 2018, DOI: 10.1016/j.jscs.2018.10.001.
10 M. Ji, X. Zhanga, J. Wang and S. Park, *J. Mol. Catal. A: Chem.*, 2013, **371**, 36–41.
11 R. Watanabe, K. Mukawa, J. Kojima, E. Kikuchi and Y. Sekine, *Appl. Catal., A*, 2013, **462–463**, 168–177.
12 R. Watanabe, Y. Saito and C. Fukuhara, *J. Mol. Catal. A: Chem.*, 2015, **404–405**, 57–64.
13 S. A. V. Prasad, M. Deeptya, P. N. Ramesha, G. Prasad, K. Srinivasarao, C. Srinivas, K. Vijaya Babu, E. Ranjith Kumar, N. Krisha Mohan and D. L. Sastry, *Ceram. Int.*, 2018, **44**, 10517–10524.
14 E. Hutamaningtyasa, U. Suharyanaa, A. T. Wijayantab and B. Purnama, *J. Phys.: Conf. Ser.*, 2016, **776**, 012–023.
15 T. Mathew, S. Malwadkar, S. Pai, N. Sharanappa, C. P. Sebastian, C. V. V. Satyanarayana and V. V. Bokade, *Catal. Lett.*, 2003, **91**, 217–224.
16 T. P. Braga, B. M. C. Sales, A. N. Pinheiro, W. T. Herrera, E. Baggio-Saitovitch and A. Valentini, *Catal. Sci. Technol.*, 2011, **1**, 1383–1392.
17 N. Bao, L. Shen, W. An, P. Padhan, C. H. Turner and A. Gupta, *Chem. Mater.*, 2009, **21**, 3458–3468.
18 A. L. Lopes-Moriyama, V. Madigou, C. P. Souza and C. Leroux, *Powder Technol.*, 2014, **256**, 482–489.
19 H. Hajiyani and R. Pentcheva, *ACS Catal.*, 2018, **8**, 11773–11782.
20 X. Shi, S. L. Bernasek and A. Selloni, *Surf. Sci.*, 2018, **677**, 278–283.
21 T. P. Braga, A. N. Pinheiro, C. V. Teixeira and A. Valentini, *Appl. Catal., A*, 2009, **366**, 193–200.
22 Y. Qiao, C. Miao, Y. Yue, Z. Xie, W. Yang, W. Hua and Z. Gao, *Microporous Mesoporous Mater.*, 2009, **119**, 150–157.
23 A. H. Batista, F. F. Sousa, S. B. Honorato, A. P. Ayala, J. M. Filho, F. W. de Sousa, A. N. Pinheiro, J. C. S. Araujo, R. F. Nascimento, A. Valentini and A. C. Oliveira, *J. Mol. Catal. A: Chem.*, 2010, **315**, 86–98.
24 S. Wong, H. Lin and C. Mou, *Appl. Catal., A*, 2000, **198**, 103–114.
25 E. Rossetto, B. P. Nicola, R. F. de Souza, K. B. Gusmão and S. B. C. Pergher, *J. Catal.*, 2015, **323**, 45–54.
26 JCPDS-ICCD Database, *The International Center of Diffraction Data*, version 2.4, 2003.
27 A. C. Larson and R. B. V. Dreele, *General Structure Analysis System (GSAS). Los Alamos National Laboratory report LAUR*, 2004, pp. 86–748.
28 B. H. Toby, *J. Appl. Crystallogr.*, 2001, **34**, 210–213.
29 L. V. Azaroff, *Elements of X-ray Crystallography*, McGraw-Hill, USA, 1968.
30 A. D. J. Becke, *Chem. Phys.*, 1993, **98**, 1372.
31 R. Dovesi, V. R. Saunders, C. Roetti, , R. Orlando, C. M. Zicovich-Wilson, F. Pascale, B. Civalleri, K. Doll, N. M. Harrison, I. J. Bush, P. D'Arco, M. Llunell, M. Causà, Y. Noël, L. Maschio, A. Erba, M. Rerat and S. Casassa, *CRYSTAL17 User's Manual*, University of Torino, Torino, 2017.
32 A. Erba, J. Baima, I. Bush, R. Orlando and R. Dovesi, *J. Chem. Theory Comput.*, 2017, **13**, 5019–5027.
33 S. Grimme, J. Antony, S. Ehrlich and H. Krieg, *J. Chem. Phys.*, 2010, **132**, 154104.

34 *CRYSTAL - Basis Sets Library*, http://www.crystal.unito.it/basis-sets.php, Accessed: 2018-11-30.
35 J. H. Stenlid and T. Brinck, *J. Am. Chem. Soc.*, 2017, **139**, 11012–11015.
36 J. Lee and S. Kwak, *ACS Omega*, 2018, **3**, 2634–2640.
37 N. I. Cuello, V. R. Elías, C. E. R. Torres, M. E. Crivello, M. I. Oliva and G. A. Eimer, *Microporous Mesoporous Mater.*, 2015, **203**, 106–115.
38 I. Ursachi, A. Stancu and A. Vasile, *J. Colloid Interface Sci.*, 2012, **377**, 184–190.
39 N. I. Cuello, V. R. Elías, C. E. R. Torres, M. E. Crivello, M. I. Oliva and G. A. Eimer, *Microporous Mesoporous Mater.*, 2015, **203**, 106–115.
40 H. T. Teo, W. R. Siah and L. Yuliati, *J. Taiwan Inst. Chem. Eng.*, 2016, **65**, 591–598.
41 D. Yun, C. Krutpijit, B. Jongsomjit and J. E. Herrera, *Surf. Sci.*, 2018, **677**, 203–212.
42 Q. Men, Z. Wang, X. Chai, Z. Weng, R. Ding and L. Dong, *Appl. Surf. Sci.*, 2016, **368**, 303–308.
43 D. Yana, H. Zhaoa, J. Peia and X. Wang, *Mater. Res. Bull.*, 2018, **101**, 100–106.
44 P. Chandramohan, M. P. Srinivasan, S. Velmurugan and S. V. Narasimhan, *J. Solid State Chem.*, 2011, **184**, 89–96.
45 O. Vozniuk, C. Bazzo, S. Albonetti, N. Tanchoux, F. Bosselet, J. M. Millet, F. D. Renzo and F. Cavani, *ChemCatChem*, 2017, **9**, 2219–2230.
46 V. Georgiadou, V. Tangoulis, I. Arvanitidis, O. Kalogirou and C. Dendrinou-Samara, *J. Phys. Chem. C*, 2015, **119**, 8336–8348.
47 B. D. Cullity and C. D. Graham, *Introduction to Magnetic Materials*, IEEE Press-Wiley, 2009.
48 J. L. Dormann, J. R. Cui and C. Stella, *J. Appl. Phys.*, 1985, **57**, 4283.
49 A. D. Arelaro, L. M. Rossi and H. R. Rechenberg, *J. Phys.: Conf. Ser.*, 2010, **217**, 012–126.
50 K. Haneda and A. H. Morrish, *J. Appl. Phys.*, 1988, **63**, 4258.
51 J. Li, M. Xu, Gang Yao and B. Lai, *Chem. Eng. J.*, 2018, **348**, 1012–1024.
52 M. Nasiria, P. Sangpoura, S. Yousefzadeh and M. Bagheri, *J. Environ. Chem. Eng.*, 2019, **7**, 102999.
53 D. Schroeer and R. C. Nininger, *Phys. Rev. Lett.*, 1967, **19**, 632.
54 A. T. Ngo, P. Bonville and M. P. Pileni, *J. Appl. Phys.*, 2001, **89**, 15.
55 B. Pawelec, L. Daza, J. L. G. Fierro and J. A. Anderson, *Appl. Catal., A*, 1996, **145**, 307.
56 T. P. Braga, A. N. Pinheiro, C. V. Teixeira and A. Valentini, *Appl. Catal., A*, 2009, **366**, 193–200.
57 J. P. Jacobs, A. Maltha, J. G. H. Reintjes, J. Drimal, V. Ponec and H. H. Brongersma, *J. Catal.*, 1994, **147**, 294.
58 A. Urda, A. Herraïz, Á. Rédey and I. Marcu, *Catal. Commun.*, 2009, **10**, 1651–1655.
59 J. Thomas, N. Thomas, F. Girgsdies, M. Beherns, X. Huang, V. D. Sudheesh and V. Sebastian, *New J. Chem.*, 2017, **41**, 7356.
60 S. Deng, S. Li, H. Li and Y. Zhang, *Ind. Eng. Chem. Res.*, 2009, **48**, 7561–7566.
61 I. Rossetti, E. Bencini, L. Trentini and L. Forni, *Appl. Catal., A*, 2005, **292**, 118–123.
62 T. Mathew, B. B. Tope, N. R. Shiju, S. G. Hegde, B. S. Rao and C. S. Gopinath, *Phys. Chem. Chem. Phys.*, 2002, **4**, 4260–4267.
63 B. Chakraborty and B. Viswanathan, *Catal. Today*, 1999, **49**, 253–260.
64 K. Hadjiivanov, J. Saussey, J. L. Freysz and J. C. Lavalley, *Catal. Lett.*, 1998, **52**, 103–108.
65 F. Caron, M. Rivallan, S. Humbert, A. Daudin and S. Bordiga, *J. Catal.*, 2018, **361**, 62–72.
66 Q. Wu, G. Mul and R. Krol, *Energy Environ. Sci.*, 2011, **4**, 2140.
67 T. Boningari, S. M. Pavani, P. R. Ettireddy, S. S. C. Chuang and P. G. Smirniotis, *Mol. Catal.*, 2018, **451**, 33–42.
68 Z. Jiang, W. Zhang, W. Shangguan, X. Wu and Y. Teraoka, *J. Phys. Chem. C*, 2011, **115**, 13035–13040.
69 M. Busch, V. Mehar, L. R. Merte, M. Shipilin, E. Lundgren, J. F. Weaver and H. Grönbeck, *Chem. Phys. Lett.*, 2018, **693**, 84–87.
70 K. Nishida, I. Atake, D. Li, T. Shishido, Y. Oumi and T. Sano, *Appl. Catal., A*, 2008, **337**, 48–57.
71 L. Xing-yi, Z. Yong and Y. Ling, *J. Fuel Chem. Technol.*, 2014, **42**, 1087–1092.
72 M. Popova, A. Szegedi, K. Lazar and Z. Karoly, *Microporous Mesoporous Mater.*, 2012, **151**, 180–187.
73 O. Shekhah, W. Ranke and R. Schlögl, *J. Catal.*, 2004, **225**, 56–68.
74 Z. Zhao, G. Ge, W. Li, X. Guo and G. Wang, *Chin. J. Catal.*, 2016, **37**, 644–670.
75 A. Kotarba, W. Bieniasz, P. Kuśtrowski, K. Stadnicka and Z. Sojka, *Appl. Catal., A*, 2011, **407**, 100–105.
76 B. B. Tope, R. J. Balasamy, A. Khurshid, L. A. Atanda, H. Yahiro, T. Shishido and S. S. Al-Khattaf, *Appl. Catal., A*, 2011, **407**, 118–126.
77 H. Lee, J. C. Jung, H. Kim, Y.-M. Chung, T. J. Kim, S. J. Lee, S. H. Oh, Y. S. Kim and I. K. Song, *Catal. Lett.*, 2008, **124**, 364.
78 Y. Joseph, M. Wühn, A. Niklewski, W. Ranke, W. Weiss, C. Wöll and R. Schlögl, *Phys. Chem. Chem. Phys.*, 2000, **2**, 5314–5319.
79 C. Kuhrs, Y. Arita, W. Weiss, W. Ranke and R. Schlögl, *Top. Catal.*, 2001, **14**, 1–4.
80 L. Zhang, Z. Wu, N. C. Nelson, A. D. Sadow, I. I. Slowing and S. H. Overbury, *ACS Catal.*, 2015, **5**, 6426–6435.
81 M. V. Ushakov, B. Senthilkumar, R. Kalai Selvan, I. Felner and M. I. Oshtrakh, *Mater. Chem. Phys.*, 2017, **202**, 159–168.
82 R. Pochamoni, A. Narani, M. Varkolu, M. D. Gudimella, S. S. P. Potharaju, D. R. Burri and S. R. R. kamaraju, *J. Chem. Sci.*, 2015, **127**, 701–709.
83 E. C. Tyo, C. Yin, M. D. Vece, Q. Qian, G. Kwon and S. Vajda, *ACS Catal.*, 2012, **2**, 2409–2423.
84 N. Y. Dzade, A. Roldan and N. H. de Leeuw, *Minerals*, 2014, **4**, 89–115.

